



1 **Quasi-10-day wave activity in the southern high-latitude MLT**
2 **region and its relation to the large-scale instability and**
3 **gravity wave drag**

4

5 Wonseok Lee¹, In-Sun Song¹, Byeong-Gwon Song¹, Yong Ha Kim²

6

7 ¹Department of Atmospheric Sciences, Yonsei University, Seoul 03722, South Korea

8 ²Department of Astronomy and Space Science, Chungnam National University,

9 Daejeon 34134, South Korea

10

11 *Correspondence to:* In-Sun Song (songi@yonsei.ac.kr)

12



13 **Abstract.** Seasonal variation of westward-propagating quasi-10-day wave (Q10DW) in
14 the mesosphere and lower thermosphere of the Southern Hemisphere (SH) high-latitude
15 regions is investigated using meteor radar (MR) observations for the period of 2012–
16 2016 and Specified Dynamics (SD) version of the Whole Atmosphere Community
17 Climate Model (WACCM). The phase difference of meridional winds measured by two
18 MRs located in Antarctica gives observational estimates of the amplitude and phase of
19 Q10DW with zonal wavenumber 1 (W1). The amplitude of the observed Q10DW-W1 is
20 large around equinoxes. In order to elucidate the variations of the observed Q10DW-W1
21 and its possible amplification mechanism, we carry out two SD-WACCM experiments
22 nudged towards the MERRA-2 reanalysis from the surface up to ~60 km (EXP60) and
23 ~75 km (EXP75). Results of the EXP75 indicate that the observed Q10DW-W1 can be
24 amplified around the barotropic/baroclinic instability regions in the middle mesosphere
25 around 60°S–70°S. In the EXP60, it is also found that Q10DW-W1 is amplified around
26 the instability regions, but the amplitude is too large compared with MR observations.
27 The large-scale instability in the EXP60 in the SH summer mesosphere is stronger than
28 that in the EXP75 and Microwave Limb Sounder observation. The larger instability in
29 the EXP60 is related to the large meridional and vertical variations of polar mesospheric
30 zonal winds in associated with gravity wave parameterization (GWP). Given
31 uncertainties inherent in GWP, these results can suggest that it is possible for models to
32 spuriously generate traveling planetary waves such as Q10DW, especially in summer,
33 due to the excessively strong large-scale instability in the SH high-latitude mesosphere.



34 **1 Introduction**

35 A series of Rossby normal modes (free oscillations) is the homogeneous solution
36 of the governing equations on a sphere linearized with respect to the isothermal and
37 quiescent reference atmosphere (e.g., Andrews et al., 1987; Forbes et al., 1995; Salby,
38 1984). Traveling normal modes exhibit clear planetary-scale spatiotemporal oscillations
39 throughout the whole atmosphere, and for sufficiently large amplitudes, these traveling
40 planetary waves (PWs) can play an important role in the momentum and energy transfer
41 to the mean flow (Salby, 1984). Three gravest traveling normal modes have been
42 observed: Westward-propagating zonal-wavenumber-1 PWs with periods of
43 approximately 5, 10, and 16 days. The classical wave theory based on the isothermal
44 and quiescent atmosphere gives the theoretical periods of 5, 8.3, and 12.5 day, but the
45 periods in the real atmosphere can be shifted to values close to 5, 10, and 16 days,
46 respectively (Salby, 1981a, b), due to influences of the vertical and meridional variation
47 of the mean horizontal winds and temperature.

48 Among the gravest modes, the quasi-5-day wave (Q5DW) and quasi-16-day
49 wave (Q16DW) have extensively been studied through observations, modeling, and
50 assimilation products: Ground-based observations (e.g., Day and Mitchell, 2010; He et
51 al., 2020; Mitra et al., 2022), satellite observations (e.g., Forbes and Zhang, 2017;
52 Huang et al., 2022), reanalysis data (e.g., Huang et al., 2017), and simulations (e.g., Qin
53 et al., 2021). Using meteor radars (MRs) located in the northern and southern polar
54 regions, Day and Mitchell (2010) showed that PW activity is strong during winter and
55 the seasonal variation of PW is similar in both polar regions. According to Qin et al.
56 (2021) and Mitra et al. (2022), the barotropic and baroclinic instabilities are the possible



57 sources of Q5DW and Q16DW in that the waves can draw energy from the mean flow
58 in the instability region. The disturbance of zonal-mean flow frequently occurs during
59 the large-scale meteorological events such as sudden stratospheric warming (SSW). It
60 has been reported that the amplitude of Q5DW or Q16DW increases during SSW events
61 (Eswaraiah et al., 2016; Lee et al., 2021; Li et al., 2021; Ma et al., 2022). In addition,
62 the amplified PWs can modulate the periods of tides through the in-situ nonlinear
63 interaction, resulting ionospheric disturbances during SSW (e.g., Goncharenko et al.,
64 2020; Forbes et al., 2021; Liu et al., 2021; Qin et al., 2019).

65 In contrast, the westward propagating quasi-10-day wave (Q10DW) with zonal
66 wavenumber 1 (W1) has received little attention compared to the other gravest normal
67 modes. Forbes and Zhang (2015) showed that Q10DW-W1 has a mean period of $9.8 \pm$
68 0.4 days using the temperature measurements from the Sounding of the Atmosphere
69 using Broadband Emission Radiometry (SABER) instrument mounted on NASA's
70 TIMED (Thermosphere Ionosphere Mesosphere Energetics Dynamics) satellite in
71 2002–2013. They presented that the large amplitude of Q10DW-W1 is found in the
72 high-latitude mesosphere and lower thermosphere (MLT) region of both hemispheres in
73 equinoxes, although their results are limited to the latitude of 50° because of the yaw
74 cycle of the satellite. Hirooka (2000) reported that the global structure of Q10DW-W1
75 using the Improved Stratosphere and Mesospheric Souder (ISAMS) instrument aboard
76 Upper Atmosphere Research Satellite (UARS) from November 1991 to May 1992. The
77 results also showed that the Q10DW-W1 is active during equinoxes and winter at 0.1
78 hPa (~ 65 km). In addition, it is found that nonuniform and background zonal wind field
79 can influence the structure of the wave in the mesosphere. The amplitude of the
80 Q10DW-W1 is uniform or decays in the vertical near the mesopause, and it does not



81 increase above the mesosphere, even though the critical layer is absent. Using the
82 airglow intensities simulated by the global circulation model assimilated by the
83 reanalysis data from ground to 30 km, Egito et al. (2017) also found that the 10-day
84 oscillation is dominant from autumn to spring in the mid-latitude MLT region. More
85 recently, Huang et al. (2021) investigated the Q10DW activity based on the Modern-Era
86 Retrospective analysis for Research and Applications version 2 (MERRA-2) reanalysis
87 data. They showed that the dominant components of Q10DW are westward-propagating
88 wave with zonal wavenumber 1 during winter and spring in the stratosphere and
89 mesosphere and eastward-propagating waves with zonal wavenumber 1 and 2, which
90 are excited in the mesospheric instability region. Although both westward and eastward
91 Q10DW modes are found, they mainly focus on the eastward propagating Q10DW.

92 Some studies have investigated the climatological and general properties of
93 Q10DW-W1 activities in the mid- and low-latitudes, but their seasonal variation in the
94 high-latitude MLT region has not been fully explored. In addition, the amplification
95 mechanism of Q10DW-W1 still has not been investigated. In the present study, we
96 focus on the seasonal variation of Q10DW-W1 in the Southern Hemisphere (SH) high-
97 latitude MLT region using MRs located in Antarctica. Plus, we carry out numerical
98 simulations using the Specified Dynamics version of the Whole Atmosphere
99 Community Climate Model (SD-WACCM) nudged towards MERRA-2 reanalysis data
100 in order to elucidate the observed Q10DW-W1 and its amplification mechanism.
101 Section 2 describes two MRs located in the Davis station (68.6°S, 77.9°E) and King
102 Sejong Station (KSS; 62.2°S, 58.8°W) and how we obtain Q10DW-W1 from the
103 observations. Also, the SD-WACCM experiments and Microwave Limb Sounder
104 (MLS) data used for validation are described in Section 2. Results are presented in



105 Section 3. In Section 3.1, we show seasonal variation of observed and modeled
106 Q10DW-W1 in the SH high-latitude MLT region. The amplification mechanism of
107 Q10DW is discussed in Section 3.2. Q10DW activities from SD-WACCM simulations
108 are demonstrated in Section 3.3. In Section 4, the results are summarized, and their
109 implications are discussed.

110

111 **2. Data and Method**

112 **2.1 Meteor Radars**

113 In this study, we use two MRs located in the Davis station (68.6°S, 77.9°E) and
114 King Sejong Station (KSS; 62.2°S, 58.8°W), Antarctica from 2012 to 2016. The
115 operating frequencies of both Davis and KSS MR are 33.2 MHz and the peak powers
116 are 6.8 kW and 12 kW, respectively. Details of the operation parameters of Davis and
117 KSS are summarized in Holdsworth et al. (2008) and Lee et al. (2018), respectively. A
118 large number of studies has been performed to investigate the PW or tidal activities in
119 the MLT region with a single-station measurements of horizontal winds from an MR
120 (e.g., Eswaraiah et al., 2019; Luo et al., 2021; Wang et al., 2021; Liu et al., 2022; Lee et
121 al., 2021). However, single-station analysis has a limitation in diagnosing the wave
122 propagation direction, and thus most of such studies focused on the timing of
123 occurrence and amplitude variations of wave with a particular periodicity. For detailed
124 analysis of PWs based on the Rossby normal modes, propagation directions and
125 wavenumbers need to be considered. Recently, He et al. (2018) developed a method of
126 estimating wave propagation direction and wavenumber as well as amplitude by
127 adopting Phase Differencing Technique (PDT) to longitudinally separated MR



128 observations based on the method of Walker et al. (2004). Since the longitude
129 difference (λ_{Δ}) between Davis and KSS is about 137° , it is appropriate for analyzing
130 PWs with zonal wavenumber 1 by applying the PDT. In order to estimate the zonal
131 wavenumber (s), we first make a continuous wavelet transform from the daily-mean
132 Davis and KSS MR data ($W_{(f,t)}^{Davis}$, $W_{(f,t)}^{KSS}$), respectively, using Morlet wavelet function
133 as a mother wavelet function (Torrence and Compo, 1998). Then, cross wavelet
134 spectrum $C_{(f,t)}$ is derived: $C_{(f,t)} = W_{(f,t)}^{*Davis} W_{(f,t)}^{KSS}$, where $*$ denotes the complex
135 conjugate. Using the phase difference (θ_{Δ}) obtained from $\theta_{\Delta} = \text{Arg}(C_{(f,t)})$ at a given
136 frequency and time, we estimate zonal wavenumber (s): $s = (-\theta_{\Delta}/(2\pi) + C)/\lambda_{\Delta}$. In
137 this study, we focus on the PW activity with $s = 1$, and the number of whole wave cycle
138 (C) between two stations is set to be zero (see He et al., 2018 for detailed PDT analysis).

139 Classical wave theory shows that the latitudinal structures of zonal wind and
140 meridional wind for Q10DW normal mode from the Laplace tidal equation are
141 antisymmetric and symmetric with respect to the equator, respectively (e.g., Figure 1 in
142 Yamazaki and Matthias, 2019). The magnitude of Q10DW-W1 has maxima at the
143 latitude of 25° and poles for zonal and meridional wind components, respectively.
144 Around the latitude of 65°S close to the latitudes of the two MR observation sites, the
145 normalized amplitude of Q10DW-W1 normal mode for the zonal wind is nearly zero,
146 but the normalized normal mode magnitude for the meridional wind is larger than the
147 half of the maximum magnitude for the meridional wind (Yamazaki and Matthias,
148 2019). For this reason, daily-mean meridional wind data from the MRs is used for the
149 Q10DW analysis.

150



151 2.2 SD-WACCM

152 In this study, for detailed analysis of the observed Q10DW-W1 activity and its
153 amplification mechanism, we compare observational results with Q10DW-W1
154 simulated using the Specified Dynamics (SD) version of WACCM version 4 (Marsh et
155 al., 2013). WACCM4 is a high-top (up to the lower thermosphere about 140 km)
156 atmospheric component model of the Community Earth System Model developed at the
157 National Center for Atmospheric Research. WACCM4 employs Community
158 Atmospheric Model (CAM) version 4 physics package. The default horizontal
159 resolution of WACCM4 is $1.9^{\circ} \times 2.5^{\circ}$ (lat. \times long.), and it uses the 88 hybrid sigma
160 vertical levels for the SD mode. Since we focus on the PWs such as Q10DW-W1, daily-
161 mean values from the SD-WACCM are used. In this study, two SD-WACCM
162 experiments with two different nudging depths (EXP60 and EXP75) are performed. In
163 the EXP60 and EXP75, model variables are nudged towards the MERRA-2 reanalysis
164 data from surface to about 60 km in altitude and 75 km, respectively. The MERRA-2
165 reanalysis is produced by assimilating various types of observations into the Goddard
166 Earth Observing System version 6 (GEOS6) global model (Gelaro et al., 2017). In
167 addition to conventional meteorological observations and operational satellite
168 measurements, the Earth Observing System (EOS) Aura MLS temperature data are
169 included in the assimilation procedure of the MERRA-2 above 5 hPa (~ 37 km). As a
170 result, MERRA-2 reanalysis can reflect the MLT variabilities. As suggested by
171 Brakebusch et al. (2013), nudging coefficients for EXP60 and EXP75 are 0.01 s^{-1} below
172 the altitudes of 50 km and 65 km, respectively, and they linearly decrease and become
173 zero above the altitudes of 60 km and 75 km, respectively.



174 WACCM simulation requires the data of sea surface temperature, sea ice
175 fraction, solar and geomagnetic indices, and ionization rate by energetic particle
176 precipitation (EPP) for the time period of simulations. The sea surface temperature and
177 sea ice fraction data are produced by the NOAA Optimum Interpolation (Reynolds et
178 al., 2002). The solar and geomagnetic indices are obtained from NASA GSFC/SPDF
179 OMNIWeb interface (<https://omniweb.gsfc.nasa.gov/ow.html>). The EPP ionization rate
180 is provided by the CCMI reference-C2 data for the period of 1960–2100 (Eyring et al.,
181 2013). Regarding MLT dynamics, effects of gravity wave drag (GWD) are crucial.
182 WACCM includes a suite of GWD parameterizations (Richter et al., 2010) for effects of
183 unresolved GW momentum transfer from orography (McFarlane, 1987), deep
184 convection (Beres et al., 2005), and frontal activity (Charron and Manzini, 2002). SD-
185 WACCM simulations start from January 1, 2011 and end at the end of 2016. First one-
186 year results are discarded as a spin-up, and results for 2012–2016 are compared with
187 MR observations.

188

189 **2.3 MLS**

190 For validation of Q10DW-W1 estimates obtained from MR observations, we
191 derive the geostrophic winds from geopotential height (GPH) data (version 5.1 product)
192 measured using MLS onboard the NASA's EOS Aura satellite (Schwartz et al., 2008).
193 Geostrophic wind components are computed following Matthias and Ern (2018). The
194 Aura satellite launched on July 2004 is in a sun-synchronous orbit with an altitude of
195 705 km. Spatial coverage of MLS instrument is from 82°S to 82°N with a 165 km
196 resolution along the track. The sun-synchronous orbit of Aura satellite can provide a



197 global coverage data per day with about 15 orbits. The global coverage of GPH is
198 produced using daily mean values in $5^{\circ} \times 5^{\circ}$ (lat. \times long.) grids. In this process, GPH
199 data is filtered on the basis of the recommended precision, status, quality, and
200 convergence thresholds of Version 5.0 Level 2 and 3 data quality and description
201 document (https://mls.jpl.nasa.gov/data/v5-0_data_quality_document.pdf).

202

203 **3. Results and Discussion**

204 **3.1 Seasonal variation of Q10DW-W1 in the MLT region**

205 The perturbation meridional wind for Q10DW-W1 is symmetric in latitude
206 about the equator as mentioned earlier. Therefore, in order to extract and analyze
207 Q10DW-W1, it is necessary to confirm whether the latitudinal structure of Q10DW-W1
208 has the hemispheric symmetry. Although the KSS and Davis MR observations can
209 provide information about the longitudinal propagation of Q10DW-W1, it is impossible
210 to estimate the latitudinal structure using these radars alone. In this study, the
211 meridional geostrophic winds obtained from the MLS geopotential data are used to
212 confirm the hemispheric symmetry of Q10DW-W1 estimated from MRs. The
213 amplitudes of Q10DW-W1 in the MLS are obtained using the two-dimensional Fast
214 Fourier transform (FFT) of the geostrophic meridional winds averaged over the height
215 range of 80–90 km in time (30-day sliding window) and longitude domain. The time-
216 latitude cross section of the amplitude of Q10DW-W1 derived from the MLS
217 geostrophic meridional wind averaged over the height range of 80–90 km is presented
218 in the Supplement (Fig. S1). Hereafter, the Q10DW denotes westward-propagating
219 quasi-10-day normal mode wave with zonal wavenumber 1 and the hemispheric



220 symmetry, where quasi-10-day periodicity means the periods between 9 and 11 days.
221 Unless the hemispheric symmetry is satisfied, the analyzed westward propagating
222 signals with zonal wavenumber 1 are referred to as quasi-10-day-like oscillations
223 (Q10DOs).

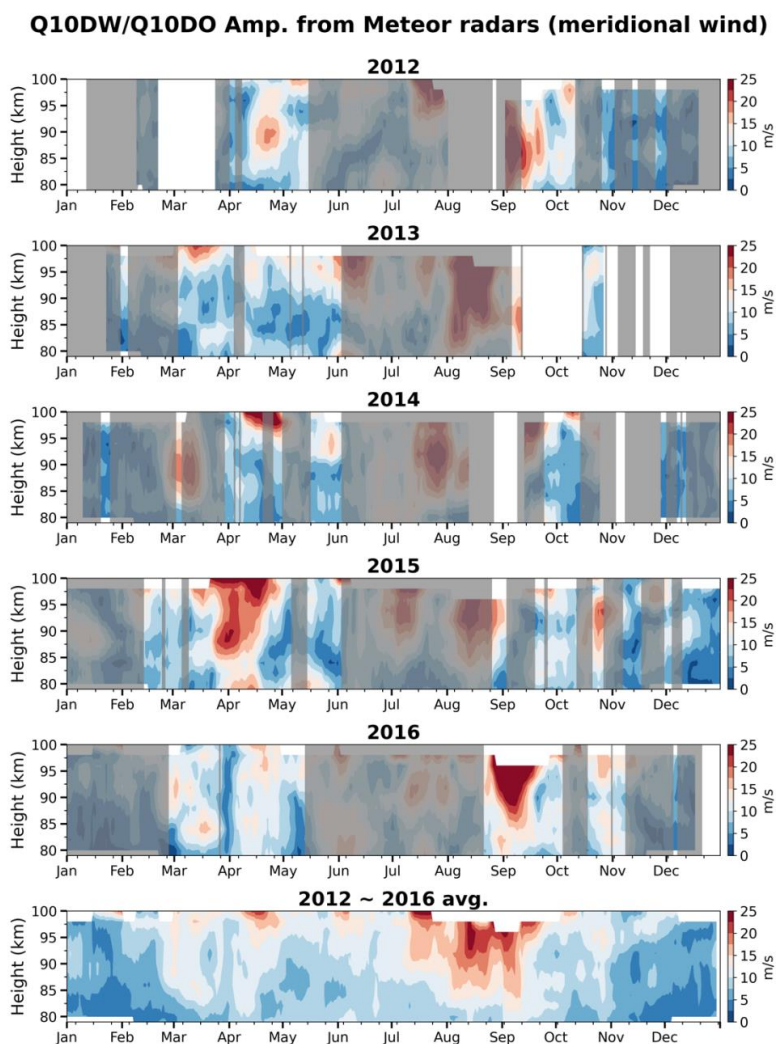
224 Figure 1 shows the time-height distributions of the amplitudes of Q10DWs and
225 Q10DOs derived from the daily-mean meridional winds observed at the Davis and KSS
226 MRs using the PDT method. The regions shaded in gray represent the time periods
227 when the hemispheric symmetry is not found in the MLS results as shown in Fig. S1.
228 The time periods of the hemispheric symmetries are defined by the periods when the
229 amplitudes of the MLS meridional geostrophic winds (vertically averaged over 80–90
230 km) with quasi-10-day periodicity exceed 3.5 m s^{-1} in both 60°N – 80°N and 60°S – 80°S .
231 The MLS results in solstices are generally shaded in gray (see Fig. S1). This result
232 indicates that Q10DWs in a form of normal modes are found during equinoxes, which is
233 consistent with the results from Forbes and Zhang (2015). Using the periods of the
234 hemispheric symmetry of the Q10DW obtained from the MLS, we identify the normal
235 mode Q10DW from the Davis and KSS MR observations.

236 The 5-yr average (The bottom-most panel of Fig. 1) between 2012 and 2016
237 indicates that the Q10DWs are generally enhanced from late February to April and from
238 late August to September in the altitude range of 82–98 km with the maximum
239 amplitude of 27.2 m s^{-1} . The Q10DWs are usually more amplified in early spring from
240 late August to September with the largest amplitudes around the altitudes of 90–95 km.
241 Large amplitudes are found in winter (July to mid-August), but they are unlikely to
242 represent the normal mode Q10DWs, as it is clear from the gray shading in winter.
243 According to Wang et al. (2021), the nonlinear wave-wave interaction can generate



244 Q10DOs in southern winter. Their Q10DOs are eastward propagating, interacting with
245 stationary PWs with zonal wavenumber 1. Meanwhile, the Q10DWs and Q10DOs (Fig.
246 1) obtained from two MRs using the PDT method are westward propagating.
247 Understanding of the mechanisms of the winter-time westward-propagating Q10DOs is
248 beyond the scope of this study, and it requires continuing researches.

249 For individual years, it is also found that the amplitude of Q10DW is generally
250 large in equinoxes (see panels for each year in Figs. 1 and S1). During March–April
251 (autumn), active Q10DWs are identified, and their amplitudes reach up to $\sim 33 \text{ m s}^{-1}$ in
252 2014 and 2015. Particularly, the peak in September (spring) is prominent in 2016. These
253 MR observation results are remarkably consistent with results obtained using satellite
254 geopotential height in the SH high-latitude region (Forbes and Zhang, 2015).
255 Occasionally, large amplitude Q10DWs are observed near the altitude of 98–100 km in
256 equinoxes (e.g., April 2015), but results around 100 km can be less reliable because the
257 number of MR echoes above 96 km is much smaller than that around 90 km (Lee et al.,
258 2022).



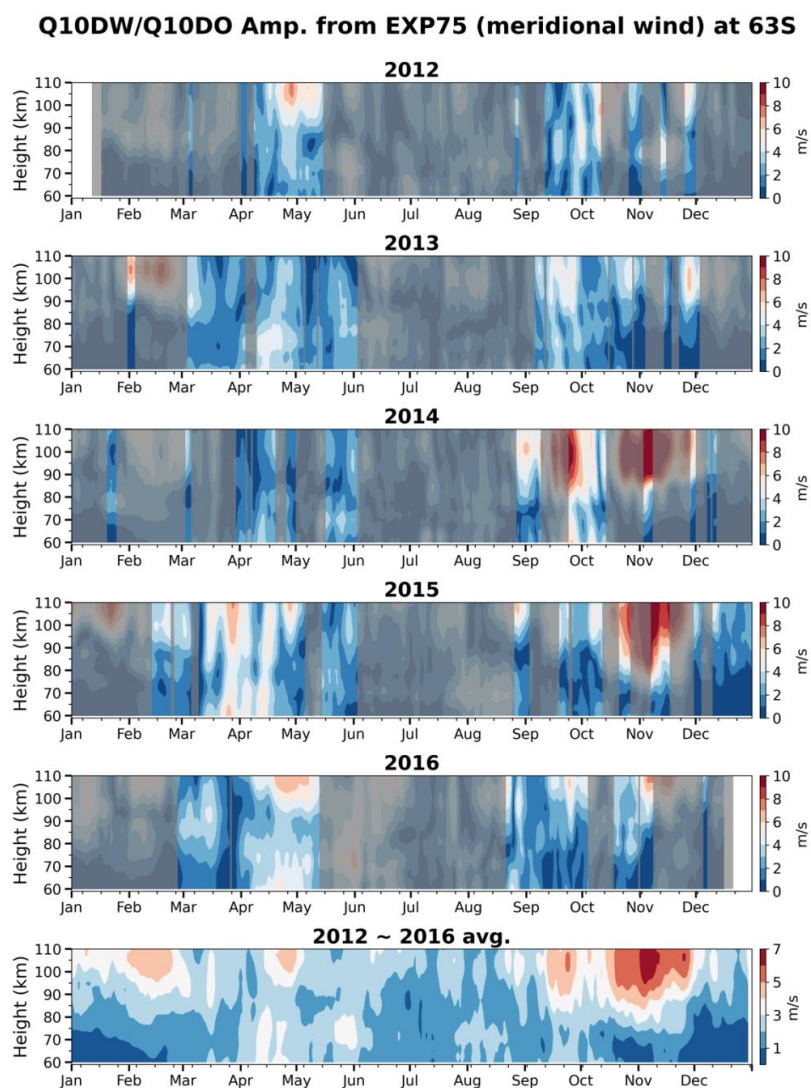
259

260 **Figure 1.** Time-height distributions of the amplitudes of Q10DWs (unshaded region)
261 and Q10DOs (shaded region) derived from meridional winds observed by MRs at Davis
262 and KSS for 2012–2016. The bottom-most panel shows the 5-yr average from 2012 to
263 2016. The gray shading represents time periods where the hemispheric symmetry is
264 unclear in the MLS results.



265 Figure 2 demonstrates the time-height distributions of the amplitudes of
266 Q10DWs and Q10DOs around the latitude of 63°S in the EXP75 SD-WACCM
267 simulation for the altitude range of 60–110 km for 2012–2016, along with the
268 hemispheric symmetry period obtained from the MLS results. The bottom-most panel of
269 Fig. 2 shows the 5-yr average from 2012 to 2016. The amplitudes are obtained by
270 decomposing the meridional winds obtained from the simulation into westward
271 propagating Fourier modes with zonal wavenumber 1 using the 2D FFT in time (30-day
272 sliding window) and longitude domain around 63°S. From Fig. 2, it is clear that the
273 seasonal variations of Q10DW amplitudes obtained from the simulation have year-to-
274 year variations, as in the Q10DW amplitudes derived from the two MRs. However, the
275 Q10DW activities observed from the MR observations are generally larger than those in
276 the EXP75 simulation (see Fig. 1).

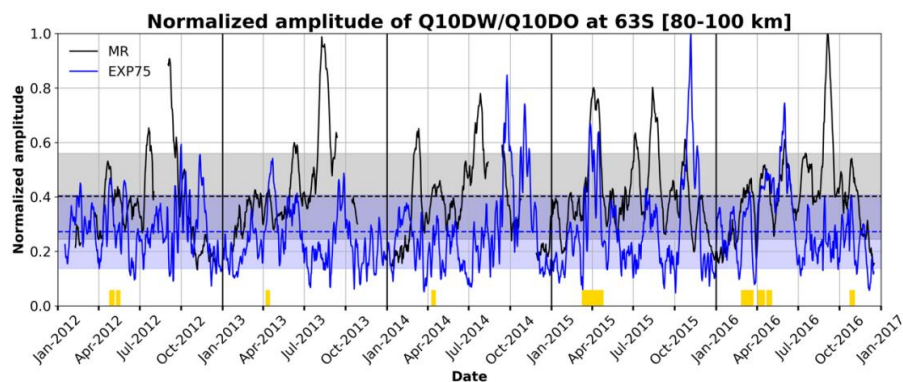
277 The 5-yr average in Fig. 2 shows that there are four main time periods
278 (February, April, September, November) when the modeled Q10DWs and Q10DOs are
279 active in the EXP75. The time periods in April and September are consistent with the
280 MR observations in terms of Q10DW amplitudes and the hemispheric symmetry
281 obtained from the MLS, but the other periods are not. The active signals simulated in
282 February and November do not appear to be normal mode Q10DWs because the
283 hemispheric symmetry is not seen in the MLS data during February and November. For
284 a more comprehensive understanding of the Q10DOs in the EXP75 during February and
285 November, we will discuss in more detail later in Section 3.3 by comparing between the
286 EXP75 and EXP60.



288 **Figure 2.** Time-height distributions of the amplitudes of Q10DWs (unshaded region)
289 and Q10DOs (shaded region) around 63°S for 2012–2016 in the EXP75. The bottom-
290 most panel shows the 5-yr average between 2012 and 2016. The gray shaded areas
291 represent periods where the hemispheric symmetry is not observed in the MLS results.



292 Figure 3 shows time series of the normalized amplitudes of Q10DWs and
293 Q10DOs obtained from the MR observations (black) and EXP75 simulation (blue).
294 Normalization is carried out by averaging the amplitudes in the altitude range between
295 80 and 100 km and dividing the 5-yr averaged values by the respective maximum
296 values in the same altitude range. We select the dates when (i) the amplitudes obtained
297 from both MRs and EXP75 exceed their respective 5-yr mean values, (ii) their
298 correlation is relatively large (> 0.6), and (iii) the hemispheric symmetry occurs in the
299 MLS results. The correlation coefficients are computed for sliding 7-day windows with
300 1-day step. The dates when the three criteria are satisfied are represented by yellow
301 boxes on abscissa in Fig. 3. The total number of the dates when the Q10DW was
302 substantially active in both observations and model (EXP75) is 46. Using EXP75 results
303 on the selected dates, the amplification mechanisms of the observed Q10DW will be
304 discussed.



305

306 **Figure 3.** Time series of normalized amplitudes of Q10DW/Q10DOs from the
307 observations (black line) and EXP75 simulation (blue line). The dashed lines and
308 shaded areas represent the mean and standard deviation of normalized amplitude of
309 Q10DW/Q10DOs from the observations (black) and EXP75 (blue), respectively.
310 Yellow boxes on abscissa indicate the dates when the normalized amplitudes from both
311 MRs and EXP75 can be considered to be those of the normal mode Q10DWs.



312 3.2 Amplification mechanisms of Q10DW

313 The amplitude of upward propagating PWs grows with height when their
314 vertical propagation is allowed, but it can decrease with height in the evanescent region
315 where the square of refractive index n^2 becomes negative. Regions of negative n^2 are
316 often accompanied by regions of the negative latitudinal gradient of zonal-mean
317 potential vorticity (\bar{q}_ϕ), where \bar{q} is the zonal-mean quasi-geostrophic potential vorticity
318 (QGPV), the overbar denotes zonal averaging, ϕ is the latitude, and the subscript ϕ
319 denotes the partial derivative in the latitudinal direction. In the regions of negative \bar{q}_ϕ ,
320 the barotropic and baroclinic instabilities can occur (Matsuno, 1970), and it is known
321 that PWs can amplify extracting energy from the mean flow while they pass through the
322 instability regions (Meyer and Forbes, 1997; Cohen et al., 2013). If PWs somehow
323 reach their critical lines within an instability region, it is possible for these PWs to
324 tunnel through the critical lines (Rhodes et al., 2021). In case that the evanescent region
325 is thin enough, and the PWs can reach their critical lines, it is also possible for the
326 overreflection to take place, resulting in the amplified PWs and the propagation of the
327 amplified PWs out of the over-reflection region (Lindzen et al., 1980; Rhodes et al.,
328 2021).

329 Another possible way of modulating PWs is their excitation by the
330 nonconservative GW forcing (Song et al., 2020). Nonconservative GWD forcing
331 (NCGWD; Z') can generate PWs as it is clearly seen from the perturbation QGPV
332 equation given in the form of wave action conservation equation (1) when diabatic
333 forcing is ignored in Z' [see Andrews et al. (1987) and Palmer (1982) for details]:
334



$$335 \quad \frac{\partial A}{\partial t} + \nabla \cdot \mathbf{F} = \rho_0 \overline{Z' q'_{(M)}} / (\bar{q}_\phi / a), \quad (1)$$

336

337 where a is the earth's mean radius; ρ_0 is the reference density given as an exponentially
 338 decreasing function of log-pressure height z ; the prime denotes the perturbation from the
 339 respective zonal mean; A is the wave-activity density in the spherical QG system; $q'_{(M)}$ is
 340 the perturbation of modified QGPV, modified to consider the planetary vorticity
 341 advection by the isallobaric meridional wind in spherical geometry (Matsuno, 1970;
 342 Palmer, 1982); Z' is the curl of the horizontal GWD perturbation; $\nabla \cdot \mathbf{F}$ is the divergence
 343 of Eliassen-Palm (EP) flux (\mathbf{F}), and the flux \mathbf{F} is considered to be the wave-activity flux
 344 given by $\mathbf{F} = \mathbf{c}_g A$ in the QG framework, where \mathbf{c}_g is the group velocity in the latitude-
 345 height domain.

346 In (1), the wave-activity density A and the modified QGPV perturbation $q'_{(M)}$ are
 347 given in spherical geometry (Palmer, 1982), respectively, as follows:

348

$$349 \quad A = a \cos \phi \frac{1}{2} \rho_0 \frac{\overline{q'^2_{(M)}}}{\bar{q}_\phi / a}, \quad (2)$$

$$350 \quad q'_{(M)} = \frac{v'_\lambda}{a \cos \phi} - \frac{f}{a \cos \phi} \left(\frac{u' \cos \phi}{f} \right)_\phi + \frac{f}{\rho_0} \left(\rho_0 \frac{\theta'}{\theta_z} \right)_z, \quad (3)$$

351

352 where u and v are zonal and meridional wind components, respectively; λ is the
 353 longitude; f is the Coriolis parameter; θ is the potential temperature. The subscript λ and
 354 z mean the partial derivatives in longitude and vertical directions, respectively.



355 For understanding of amplification of PWs around the instability regions, the
356 barotropic and baroclinic instability regions are determined by the negative sign of \bar{q}_ϕ
357 (Andrews et al. 1987) given by:

358

$$359 \quad \bar{q}_\phi = 2\Omega \cos \phi - \left[\frac{(\bar{u} \cos \phi)_\phi}{a \cos \phi} \right]_\phi - \frac{a}{\rho_0} \left(\frac{\rho_0 f^2}{N^2} \bar{u}_z \right)_z, \quad (4)$$

360

361 where Ω is the earth's rotation rate and N is the buoyancy frequency. The negative sign
362 of \bar{q}_ϕ is a necessary condition of the barotropic and baroclinic instabilities. The second
363 (with negative sign) and third (with negative sign) terms on the right-hand side of (4)
364 represent the meridional and vertical curvatures of the zonal-mean zonal wind,
365 respectively. If the second or third term is dominant, \bar{q}_ϕ can become negative, and the
366 instabilities can take place.

367 The square of refractive index n^2 is used to analyze the propagation
368 characteristics of PWs and depends on the mean QGPV gradient as follows:

369

$$370 \quad n^2 = \frac{\bar{q}_\phi}{a(\bar{u}-c)} - \frac{s^2}{a^2 \cos^2 \phi} - \frac{f^2}{4N^2 H^2}, \quad (5)$$

371

372 where c is the zonal phase speed of single PW (i.e., $c = 2\pi a \cos \phi / (s\tau)$; s is the zonal
373 wavenumber, and τ is the wave period), and the constant scale height H is set equal to 7
374 km. The propagation of PWs is possible in regions of positive n^2 . On the other hand,
375 PWs can be reflected or be evanescent in the region where $n^2 < 0$ (Matsuno, 1970).



376 In order to analyze the wave propagation and wave activity for the selected dates
377 for Q10DWs (or Q10DOs) found in MRs and model simulations, we use the EP flux as
378 diagnostic tools, derived in the Transformed Eulerian-Mean framework for the spherical
379 QG system (Palmer, 1982; Andrews et al., 1987). In the spherical geometry, the
380 meridional (F^ϕ) and vertical (F^z) components of the EP flux $\mathbf{F} \equiv (0, F^\phi, F^z)$ are given
381 by

382

$$383 \quad F^\phi = -\rho_0 a \cos \phi \overline{u'v'}, \quad (6)$$

$$384 \quad F^z = \rho_0 a \cos \phi f \overline{v'\theta'}/\bar{\theta}_z, \quad (7)$$

385

386 Figure 4 shows the EP flux \mathbf{F} and wave activity density normalized by $\rho_0 a \cos \phi$
387 for Q10DWs in the EXP75. The propagation inhibition region ($n^2 < 0$) and the
388 contours of zonal-mean zonal wind are overplotted. Thick green and black lines indicate
389 the regions of $\bar{q}_\phi = 0$ and of critical lines for Q10DWs, respectively. The critical lines
390 are plotted by computing the zonal phase speed (c) of Q10DW: $c = 2\pi a \cos \phi / (s\tau)$,
391 where $s = 1$ and $\tau = 10$ day. The wave-activity density is shaded in blue and red
392 depending on its sign. For the EP flux vector, $\mathbf{F}/\text{sgn}(A)$ ($= \mathbf{c}_g|A|$), rather than \mathbf{F} itself
393 ($= \mathbf{c}_g A$), is plotted such that the EP flux can always be parallel to the local group
394 velocity of Q10DWs regardless of the instability regions where $\bar{q}_\phi < 0$ and thus $A < 0$.
395 For better illustration of the EP flux in the atmosphere where its density decreases
396 exponentially with height, the meridional and vertical components of EP flux are scaled



397 by $(p_s/p)^{0.85}[F^\phi/(a\pi), F^z/(3 \times 10^5)]$ (Edmon et al., 1980; Gan et al., 2018), where p_s
398 and p are the surface and atmospheric pressures, respectively.

399 For Figure 4, we select the four dates of (a) 30 April 2012, (b) 11 April 2013, (c)
400 6 April 2015, and (d) 29 October 2016 when the three criteria mentioned in Fig. 3 are
401 satisfied (see yellow boxes in Fig. 3). That is, the normalized amplitudes of Q10DWs
402 from both MRs and EXP75 are larger than its average, the correlation coefficient is
403 larger than 0.6, and the hemispheric symmetry is found in the MLS results. The 30
404 April 2012 case (Fig. 4a) shows that the stratospheric jet is located around (40°S–60°S,
405 55 km) in the latitude-height domain and that there is a predominant branch of upward
406 and equatorward Q10DW EP flux vectors across the center of the stratospheric jet. In
407 the high-latitude mesosphere, there are two regions where both the large-scale
408 instability ($\bar{q}_\phi < 0$) and evanescence ($n^2 < 0$) take place, and they are located in
409 (55°S–65°S, 60–85 km) and (65°S–80°S, 70–110 km), respectively. Along the
410 instability boundaries (green lines), large positive or negative Q10DW activities are
411 found. Divergent EP flux vectors in the meridional direction are clearly seen around the
412 instability region located at (53°S, 65–75 km), which implies the excitation of Q10DWs
413 in association with the instability. In the region of MR observations (60°S–65°S, 85–
414 100 km), substantially amplified Q10DW activity appears, and the equatorward
415 Q10DW EP flux towards the MR sites is found over the amplified Q10DW activity.

416 Figures 4b demonstrates the case of 11 April 2013. One major branch of
417 Q10DW EP flux vectors (Fig. 4b) originate from the stratospheric jet located at (55°S–
418 60°S, 45–60 km). In the southern and upper side of the stratospheric jet, the instability
419 and evanescent region extends from 45 km to 70 km height in the latitude of 50°S–



420 75°S. Above the instability region, distinct region of strong wave activity is found
421 around (50°S–65°S, 65–90 km), and this region is partially overlapped by the MR
422 observation region. Around this region, the Q10DW EP flux is directed downward and
423 poleward inside of the instability region (within green line). The Q10DW EP flux is
424 directed upward and equatorward outside and above the instability region. This
425 diverging pattern of EP flux around the instability region also shows the possibility of
426 the excitation of Q10DW in association with the instability.

427 For 6 April 2015 case (Fig. 4c), the structure of wave-activity density and
428 instability regions are similar to the 30 April 2012 case (Fig. 4a). The instability and
429 evanescent regions occur around (60°S–80°S, 70–100 km). Along the instability
430 boundaries, there are strong positive and negative wave-activity densities, and this
431 region of strong wave activities includes the MR observation region. Again, the
432 divergent of Q10DW fluxes appears in the upper part of the instability region around
433 (60°S–70°S, 80–100 km). The Q10DW propagates upward and equatorward outside of
434 the instability region and downward inside of the instability region, as in the other dates
435 shown in Figs. 4a and 4b.

436 In 29 October 2016 case (Figure 4d), the center of stratospheric jet is located
437 around (60°S–70°S, 20–30 km). Above the stratospheric jet, the eastward wind turns
438 westward around the altitude of 60 km. Within the region of westward wind, the
439 instability and evanescent regions are found. In addition, the critical lines exist inside
440 the instability region. The overreflection or transmission process can take place near the
441 critical lines as we mentioned. Notably, the significantly large positive and negative
442 wave-activity density regions are found around (45°S–70°S, 60–90 km) near the



443 instability boundaries, and these regions are partially overlapped by the MR observation
444 region. This result suggests that the observed amplification of Q10DW may be
445 attributed to the overreflection or transmitted process. The EP flux of Q10DW
446 predominantly propagates upward and equatorward away from the strong wave-activity
447 region around (60°S, 60–70 km) with weak poleward propagation of Q10DW towards
448 the instability region across the critical lines.

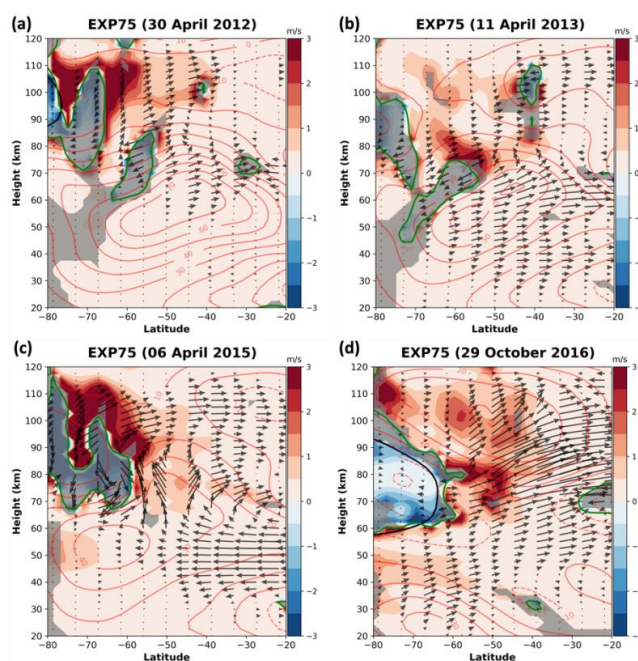
449 For all the cases shown in Fig. 4, the results indicate that a distinct strong wave-
450 activity density region is located within the area observed by the MRs (around 60°S–
451 70°S and 80–100 km in height) associated with the large-scale instability region.
452 Considering the wave-activity density A is directly proportional and inverse
453 proportional to the $\overline{q'^2}$ and \bar{q}_ϕ , respectively, it can be thought that the small \bar{q}_ϕ
454 contributes the large magnitude of A near the instability region. However, we confirm
455 that the large $\overline{q'^2}$ is located around the instability region, leading to the overall large
456 wave-activity density (not shown in here). In addition, the group velocity of the wave is
457 given by $\mathbf{c}_g = \mathbf{F}/A$. For the selected cases (Fig. 4), the EP flux \mathbf{F} in the MR observation
458 region is relatively small, while the magnitude of A is comparatively large. This
459 suggests a small group velocity in this region. These results agree with the study of
460 Thorncroft et al. (1993), which states that during the amplification of baroclinic waves,
461 the group velocity tends to be small.

462 As previously mentioned, Song et al. (2020) proposed that the NCGWD can
463 generate PWs. In this regard, the resolved GWs ($s \geq 20$) could also play a role in
464 generating Q10DW. To verify the contribution of NCGWD, we analyze linearized
465 disturbance QGPV equation (Andrews et al., 1987) for the 4 cases shown in Fig. 4. Our



466 analysis shows that the contribution of both NCGWD and resolved GW for the Q10DW
467 is negligible in the MLT region (see Fig. S3 in the Supplement).

468 These results indicate that the large amplitudes of Q10DW observed in the SH
469 high-latitude region by the Davis and KSS MRs can originate from the high-latitude
470 stratosphere-mesosphere region, where the barotropic/baroclinic instability or
471 overreflection near the critical layer occur.



472

473 **Figure 4.** EP flux parallel to local group velocity $[\mathbf{F}/\text{sgn}(A)]$ and normalized wave
474 activity density $[A(\rho_0 a \cos \phi)^{-1}]$ given in the unit of m s^{-1} for the Q10DWs in the
475 EXP75 on (a) 30 April 2012, (b) 11 April 2013, (c) 6 April 2015, and (d) 29 October
476 2016. The activity density A is shaded in blue and red depending on its sign. The
477 boundaries of the instability regions ($\bar{q}_\phi = 0$, green lines), the negative n^2 regions (grey



478 shading), and the red contours for zonal-mean zonal wind are overplotted. For eastward
479 (westward) zonal-mean zonal wind, contours are plotted in solid (dashed) lines, and
480 contour interval is 10 m s^{-1} .

481 **3.3 Comparison of Q10DO between SD-WACCM simulations**

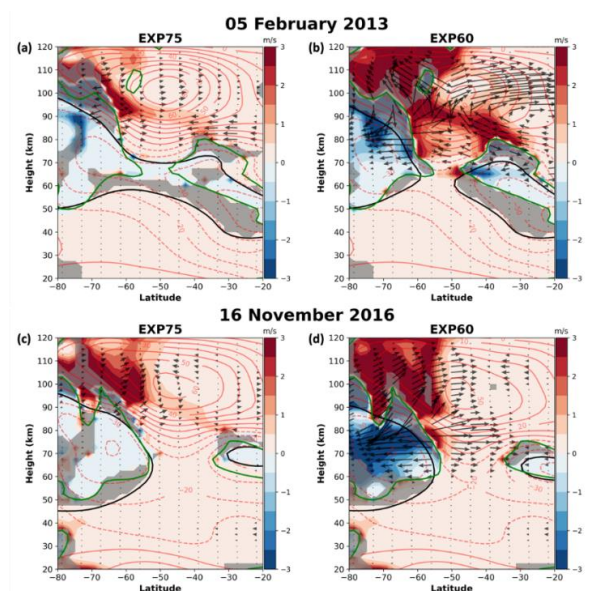
482 This section compares the Q10DOs around the mesospheric instability regions
483 in the two SD-WACCM simulations (EXP75 and EXP60) for February and November.
484 February and November are chosen because the amplitudes of modeled Q10DOs are
485 substantial. The magnitude of Q10DO in the EXP75 is generally smaller than that in the
486 EXP60, which is more comparable to the MR and MLS observations in which both
487 Q10DWs and Q10DOs are weak (see Figs. S1 and S2 in the Supplement). Note that
488 more realistic meteorological fields are nudged throughout the mesosphere in the
489 EXP75. In this section, comparison between EXP75 and EXP60 for February and
490 November is carried out to reveal mechanisms behind weak Q10DOs in the EXP75.

491 Figure 5 demonstrates the properties of Q10DO and background atmospheric
492 conditions (as shown in Figure 4) for 5 February 2013 and 16 November 2016 when the
493 Q10DO activity is found to be large in both simulations. The left and right panels of
494 Fig. 5 are the results from the EXP75 and EXP60, respectively. In Fig. 5, it is clear that
495 the strong wave-activity density for Q10DO arise in polar regions above the altitude of
496 70 km in the EXP60, and the magnitude of the EP fluxes in the EXP60 is stronger than
497 that in EXP75. In addition, in 5 February 2013 for the EXP60 (Fig. 5b), a substantially
498 strong wave-activity density region is located in the mid-latitude mesospheric region as
499 well. Around the strong wave-activity regions in the polar upper mesosphere, it is seen
500 that the EP fluxes of Q10DWs are divergent. In addition, the distinct wave-activity



501 density of Q10DO regions in the EXP60 occur along the instability regions and critical
502 lines around (50°S–70°S, 70–110 km) and (20°S–40°S, 65–80 km). On the other hand,
503 the wave-activity density of Q10DO in the EXP75 (Fig. 5a and 5c) is located at
504 relatively higher altitudes (80–100 km), and the strength of Q10DO EP flux and wave-
505 activity density are weaker than EXP60. Moreover, the negative EP flux divergence
506 (EPFD) is much larger in the EXP60 than in the EXP75 above the altitude of 80 km (not
507 shown in here).

508 Our analysis reveals that the larger wave-activity density and EP fluxes in the
509 EXP60 along the large-scale instability region in the polar upper mesosphere compared
510 to the EXP75. This indicates that the stronger large-scale instability in the EXP60 can
511 amplify Q10DO activities, which is consistent with the analysis result that the
512 barotropic and baroclinic instabilities can be the major sources of the amplification of
513 traveling PWs (Harvey et al., 2019).

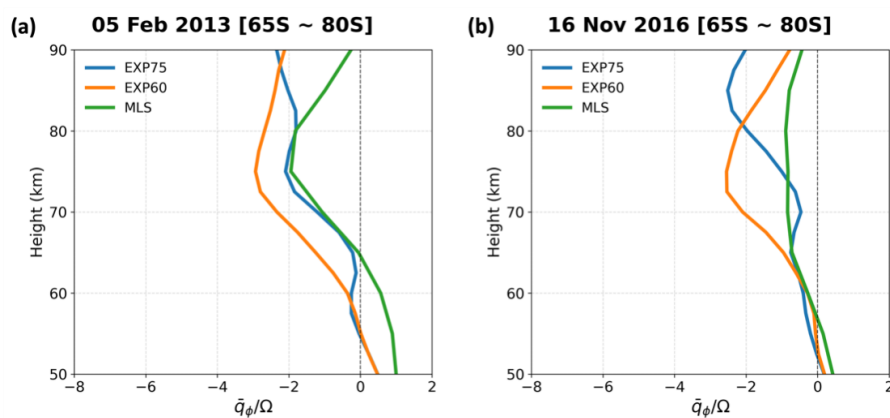


514



515 **Figure 5.** Same as Fig. 4 but for (a and b) 5 February 2013 and (c and d) 15 November
516 2016. The left and right columns represent the results from EXP75 and EXP60,
517 respectively.

518 Figure 6 shows the \bar{q}_ϕ (normalized by Ω) for 5 February 2013 and 16 November
519 2016 from the EXP75 (blue), EXP60 (orange), and MLS (green). The normalization
520 makes \bar{q}_ϕ dimensionless. The \bar{q}_ϕ/Ω from MLS is derived in the quasi-geostrophic
521 framework (Andrews et al., 1987) and it is included as a reference for validation. The
522 \bar{q}_ϕ/Ω is averaged between the latitudes of 65°S–80°S where the wave-activity density is
523 strong and large negative \bar{q}_ϕ is found in Fig. 5. It is seen that the vertical profiles of
524 \bar{q}_ϕ/Ω from the EXP75 and MLS have somewhat small negative values and they are
525 generally similar below the altitude of 75 km, although the difference gradually increase
526 above the altitude of 75 km. On the other hand, large discrepancies are shown between
527 EXP75 and EXP60 in the altitudes between 60–80 km. In the EXP60, \bar{q}_ϕ/Ω has much
528 larger negative values, which suggest the relatively stronger barotropic or baroclinic
529 instability in the EXP60 and the amplification of the Q10DO in the mid-to-upper
530 mesosphere in association with the stronger instability in the EXP60.



531

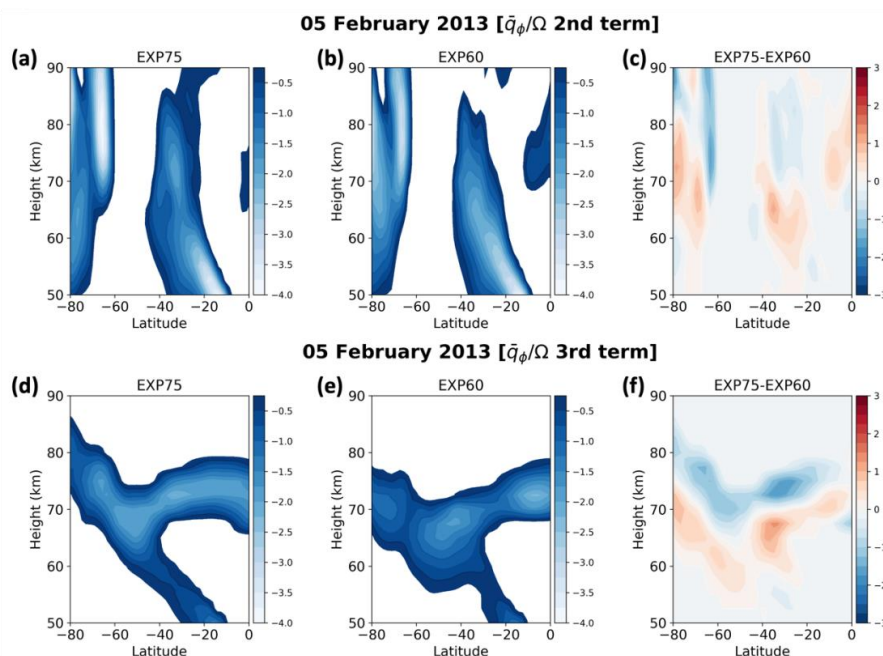
532 **Figure 6.** \bar{q}_ϕ (normalized by Ω) averaged over 65°S–85°S for (a) 5 February 2013 and
533 (b) 16 November 2016 from the EXP75 (blue), EXP60 (orange), and MLS (green).

534 The negative \bar{q}_ϕ can be induced by latitudinal and vertical curvatures of zonal-
535 mean zonal wind that correspond to the second and third terms (with negative signs) in
536 the right side of (4), respectively. Figure 7 shows the second (top panels) and third
537 (bottom panels) terms, respectively, for 5 February 2013. The difference shown in Figs.
538 7c and 7f indicate that the larger negative \bar{q}_ϕ is located in the lower altitudes in the
539 EXP60 than in EXP75, inducing the larger instability at 65–75 km in height around
540 70°S–80°S in the EXP60, which is consistent with Fig. 6. Note that the positive
541 differences seen at about 65–75 km in the high-latitude regions in Figs. 7c and 7f mean
542 the larger negative \bar{q}_ϕ in the EXP60. Also, it is clear that both vertical and horizontal
543 shear contribute the stronger barotropic/baroclinic instability in the EXP60 in the mid-
544 to-upper mesosphere, as shown in Figs. 7a-b and 7d-e. This analysis demonstrates the
545 mesospheric dynamics specified by the MERRA-2 data up to the altitude of 75 km
546 reduces the large-scale instability in the mid-to-upper mesosphere in the EXP75. This is



547 consistent with Sassi et al. (2021) proposed the absence of specification of middle
548 atmosphere dynamics induce the instability in summer mesospheric westward jet,
549 leading large traveling PWs.

550 The wind structure in the MLT region is mainly driven by momentum
551 deposition from PWs and GWs. Harvey et al. (2019) reported that GWs can change
552 significantly the vertical shears, leading enhanced instability and larger traveling PWs in
553 the mesospheric region based on the satellite observations and SD-WACCM
554 simulations. In addition, the unresolved GW forcing is one of the main factors to
555 maintain the necessary conditions of barotropic/baroclinic instability in the modeled
556 mesosphere (Sato et al., 2018). Therefore, in order to better understand the mechanisms
557 underlying the discrepancies in zonal wind fields and the resulting instability in the
558 model, it is important to examine the contribution of resolved wave forcing (EPFD) and
559 GWD forcing on the zonal wind structure in the mesosphere.



560

561 **Figure 7.** Contribution of (top) the meridional variation of the zonally-averaged mean
 562 flow and (bottom) its vertical variation in the instability condition (negative \bar{q}_ϕ) shown
 563 in (2), respectively, for 5 February 2013. Each column presents the results from (a and
 564 d) the EXP75, (b and e) the EXP60, and (c and f) difference between EXP75 and
 565 EXP60. Only negative values are plotted except for two panels for difference.

566 Figure 8 shows the latitude-height distributions of zonal-mean zonal wind, zonal
 567 component of GWD and resolved wave forcing (EPFD) in 5 February 2013 for the
 568 EXP75, the EXP60, and the difference between EXP75 and EXP60 (EXP75–EXP60).
 569 The zonal-mean zonal wind, zonal component of GWD, and resolved wave forcing
 570 (EPFD) are calculated through the 21-day averaging (central date ± 10 days). For GWD,
 571 the orographic and nonorographic values are added. In Figs. 8a–b, zero-wind lines are
 572 located around 80 km height in the SH mid-latitude region, indicating the reversal of the

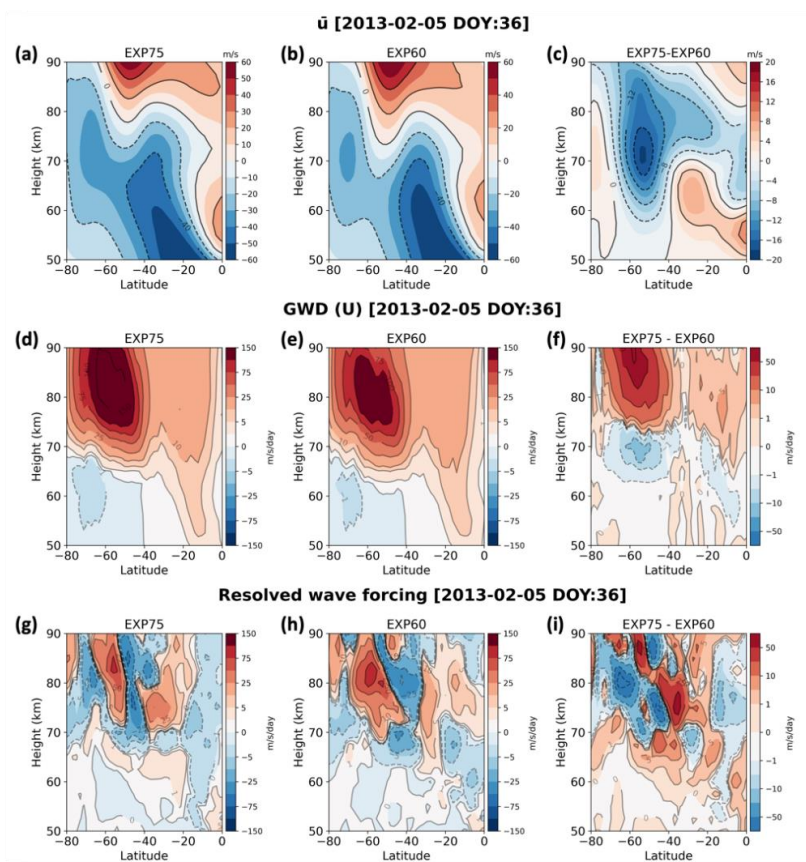


573 zonal-mean zonal wind due to the eastward momentum forcing from the GWs and
574 resolved waves. It is clear that the zero-wind line in the EXP60 is located at lower
575 altitudes by about 5 km compared to the EXP75, which means that eastward GWD and
576 eastward EPFD from the EXP60 can be larger below the altitude of ~80 km than that
577 from EXP75. Indeed, the difference field between EXP75 and EXP60 for GWD (Fig.
578 8f) shows that the eastward GWD from the EXP60 is larger around (60°S, 70 km) than
579 that from EXP75 as indicated by the negative difference field in those regions. In
580 addition, the resolved wave forcing (EP flux divergence) is more eastward above the
581 altitude of 70 km in the mid-to-high latitude regions in the EXP60 than in the EXP75.
582 This result indicates that the eastward resolved wave forcing also contributes more in
583 the mid-to-upper mesosphere in the EXP60, resulting in the zonal-mean zonal wind
584 reversal (westward to eastward wind) in the lower altitude in the EXP60.

585 As mentioned before, the amplification or modulation of westward-propagating
586 PWs with zonal wavenumber 1 and a quasi-10-day period due to NCGWD and resolved
587 GW is negligible (Fig. S3 in Supplement), indicating that the amplification of Q10DW
588 or Q10DO is mainly related to the baroclinic/barotropic instability. The stronger
589 instability in the EXP60 around the altitude of 70 km indicates that WACCM simulates
590 a large meridional and vertical variation of zonal winds compared to the observations in
591 the mid-to-upper mesosphere, which is likely due to the stronger eastward GWD and
592 eastward EPFD forcing near 70 km altitude in the EXP60, as shown in Fig. 8. Cohen et
593 al. (2013) reported that parameterized GWs can generate instability that can generate
594 resolved waves of which forcing (i.e., EPFD) can compensate GWD. Our results also
595 show that the increased eastward GWD at 70 km altitude generates instability and it
596 leads more Q10DO. The EPFD in the EXP60 gives the more eastward forcing above 70



597 km enhancing the wind reversal in the mid-to-high latitudes, but comparison of Figs. 8f
598 and 8i indicates that the compensation between GWD and EPFD is roughly valid with
599 slight shift in the vertical direction. Raising the nudging altitude of MERRA-2
600 reanalysis data to 75 km from 60 km reduces the instability in the mid-to-upper
601 mesosphere, leading to decreased the Q10DO activity in the EXP75. Therefore, we
602 suggest that strong eastward GWD in the mid-to-upper mesosphere in summer need to
603 be alleviated, which can generate more instability in the SH high-latitude mesosphere
604 region that can lead to discrepancy from observations.



605

606 **Figure 8.** Latitude-height distributions of (a–c) zonal-mean zonal wind, (d–f) zonal
607 component of GWD and (g–i) resolved wave forcing (EP flux divergence) in 5 February
608 2013 for (left) the EXP75, (middle) the EXP60, and (right) difference between EXP75
609 and EXP60 (EXP75–EXP60).

610



611 **4. Summary**

612 In this paper, the seasonal variation and the amplification mechanism of
613 Q10DW during 2012–2016 in the SH high-latitude regions are investigated using two
614 MRs located in Antarctica, and SD-WACCM simulations.

- 615 1. Using the phase difference of meridional winds measured by two MRs, we
616 extract westward-propagating Q10DW with zonal wavenumber 1. The seasonal
617 variation of the observed Q10DW shows that the amplitude is strong during
618 equinoxes, which is consistent with previous studies.
- 619 2. In order to elucidate the amplification mechanism of Q10DW observed by MRs
620 during equinoxes, two SD-WACCM experiments are carried out using the
621 MERRA-2 reanalysis data from surface to ~60 km (EXP60) and ~75 km
622 (EXP75), respectively.
- 623 3. The temporal variation of the averaged amplitude of Q10DW in the EXP75
624 during 2012–2016 is in better agreement with the MR observations.
625 Meanwhile, the amplitude of Q10DW in the EXP60 is excessive compared with
626 the observations.
- 627 4. Based on the analysis of meridional gradient of the QGPV and wave-activity
628 density, the Q10DW observed in the SH high-latitude region by the MRs
629 originated in situ around the high-latitude stratosphere-mesosphere region,
630 where the large-scale instability or overreflection near the critical lines occur.
- 631 5. The unrealistically large magnitude of Q10DO (quasi-10-day-like oscillations
632 without satisfying the hemispheric symmetry unlike Q10DW) is simulated in
633 the EXP60 during February and November. In order to reveal mechanisms of



634 the large amplitude of Q10DO in the EXP60 during the SH summer, we
635 compare the meridional gradient of QGPV from EXP75 and EXP60.
636 6. The results show that specified dynamics with MERRA-2 reanalysis data
637 mitigate the meridional and vertical variation of zonal winds in the polar mid-
638 to-upper mesosphere in the EXP75, leading reduction in the large-scale
639 instability. On the other hand, the large amplitude of Q10DO in the EXP60 is
640 attributed to the large-scale instability related to the GWD and partially to the
641 EPFD in the polar mid-to-upper mesosphere. The polar mesospheric GWD can
642 lead to a strong large-scale instability in the SH high-latitude mesosphere and
643 unrealistically large amplitude of Q10DO in summer.

644 The present study on the amplification mechanism of Q10DW during equinoxes, and
645 the unrealistic Q10DO amplitude in summer provide potential importance of large-scale
646 instability, which can be to a substantial degree caused by parameterized GWD, during
647 summer in the polar mesosphere for numerical models. In this paper, we focus on the
648 Q10DW relating to the large-scale instability and polar mesospheric GWD, but other
649 normal modes of PW will be considered for future studies.

650 **Code and Data availability**

651 The source code of Community Earth System Model 2 (CESM2) developed at
652 the National Center for Atmospheric Research (NCAR) is available at
653 <https://www.cesm.ucar.edu/models/cesm2>. The atmospheric forcing data for specified
654 dynamics are available from NCAR Research Data Archive (RDA) at
655 <https://rda.ucar.edu>.



656 The Davis station meteor radar data are available from the Australian Antarctic
657 Data Centre at https://data.aad.gov.au/metadata/records/Davis_33MHz_Meteor_Radar.
658 The King Sejong Station meteor radar data are available from Korea Polar Data Center
659 (KPDC) at <https://kpdc.kopri.re.kr>. The GPH data from the MLS onboard the NASA's
660 EOS Aura satellite are available from Goddard Earth Science Data and Information
661 Services Center (GES DISC) at <https://daac.gsfc.nasa.gov>.

662 **Author contributions**

663 WL, ISS, and YHK designed the study. WL and ISS carried out the SD-
664 WACCM experiments and analysis the observational data. WL wrote the manuscript.
665 ISS and BGS aided in interpreting the results and worked on the manuscript. All authors
666 discussed the results and contributed to the final manuscript.

667 **Competing interests**

668 The authors declare that they have no conflict of interest.

669 **Acknowledgements**

670 This research was supported by the Korea Astronomy and Space Science
671 Institute under the R&D program (Project No. 2023-1-850-07) supervised by the
672 Ministry of Science and ICT.

673



674 **References**

- 675 Andrews, D. G., Holton, J. R., and Leovy, C. B.: Middle Atmosphere Dynamics,
676 Elsevier, New York, USA, 489 pp., 1987.
- 677 Beres, J. H., Garcia, R. R., Boville, B. A., and Sassi, F.: Implementation of a gravity
678 wave source spectrum parameterization dependent on the properties of convection in the
679 Whole Atmosphere Community Climate Model (WACCM), *J. Geophys. Res.-Atmos.*,
680 110, <https://doi.org/10.1029/2004jd005504>, 2005.
- 681 Brakebusch, M., Randall, C. E., Kinnison, D. E., Tilmes, S., Santee, M. L., and
682 Manney, G. L.: Evaluation of Whole Atmosphere Community Climate Model
683 simulations of ozone during Arctic winter 2004–2005, *J. Geophys. Res.-Atmos.*, 118,
684 2673–2688, <https://doi.org/10.1002/jgrd.50226>, 2013.
- 685 Charron, M. and Manzini, E.: Gravity Waves from Fronts: Parameterization and Middle
686 Atmosphere Response in a General Circulation Model, *J. Atmos. Sci.*, 59, 923–941,
687 [https://doi.org/10.1175/1520-0469\(2002\)059<0923:gwffpa>2.0.co;2](https://doi.org/10.1175/1520-0469(2002)059<0923:gwffpa>2.0.co;2), 2002.
- 688 Cohen, N. Y. and Bühler, E. P. G. and O.: Compensation between Resolved and
689 Unresolved Wave Driving in the Stratosphere: Implications for Downward Control, *J.*
690 *Atmos. Sci.*, 70, 3780–3798, <https://doi.org/10.1175/jas-d-12-0346.1>, 2013.
- 691 Danabasoglu, G., Lamarque, J. -F., Bacmeister, J., Bailey, D. A., DuVivier, A. K.,
692 Edwards, J., Emmons, L. K., Fasullo, J., Garcia, R., Gettelman, A., Hannay, C.,
693 Holland, M. M., Large, W. G., Lauritzen, P. H., Lawrence, D. M., Lenaerts, J. T. M.,
694 Lindsay, K., Lipscomb, W. H., Mills, M. J., Neale, R., Oleson, K. W., Otto-Bliesner, B.,



- 695 Phillips, A. S., Sacks, W., Tilmes, S., Kampenhout, L., Vertenstein, M., Bertini, A.,
696 Dennis, J., Deser, C., Fischer, C., Fox-Kemper, B., Kay, J. E., Kinnison, D., Kushner, P.
697 J., Larson, V. E., Long, M. C., Mickelson, S., Moore, J. K., Nienhouse, E., Polvani, L.,
698 Rasch, P. J., and Strand, W. G.: The Community Earth System Model Version 2
699 (CESM2), *J. Adv. Model. Earth. Sy.*, 12, <https://doi.org/10.1029/2019ms001916>, 2020.
- 700 Day, K. A. and Mitchell, N. J.: The 5-day wave in the Arctic and Antarctic mesosphere
701 and lower thermosphere, *J. Geophys. Res.-Atmos.*, 1984–2012, 115,
702 <https://doi.org/10.1029/2009jd012545>, 2010.
- 703 Edmon, H. J., Hoskins, B. J., and McIntyre, M. E.: Eliassen-Palm Cross Sections for the
704 Troposphere, *J. Atmos. Sci.*, 37, 2600–2616, [https://doi.org/10.1175/1520-0469\(1980\)037<2600:epcsft>2.0.co;2](https://doi.org/10.1175/1520-0469(1980)037<2600:epcsft>2.0.co;2), 1980.
- 706 Egito, F., Takahashi, H., and Miyoshi, Y.: Effects of the planetary waves on the MLT
707 airglow, *Ann. Geophys.*, 35, 1023–1032, <https://doi.org/10.5194/angeo-35-1023-2017>,
708 2017.
- 709 Eswaraiah, S., Kim, Y. H., Hong, J., Kim, J.-H., Ratnam, M. V., Chandran, A., Rao, S.
710 V. B., and Riggan, D.: Mesospheric signatures observed during 2010 minor
711 stratospheric warming at King Sejong Station (62°S, 59°W), *J. Atmos. Sol-Terr. Phys.*,
712 140, 55–64, <https://doi.org/10.1016/j.jastp.2016.02.007>, 2016.
- 713 Eswaraiah, S., Ratnam, M. V., Kim, Y. H., Kumar, K. N., Chalapathi, G. V.,
714 Ramanajaneyulu, L., Lee, J., Prasanth, P. V., Thyagarajan, K., and Rao, S. V. B.:
715 Advanced meteor radar observations of mesospheric dynamics during 2017 minor SSW



- 716 over the tropical region, *Adv. Space. Res.*, 64, 1940–1947,
717 <https://doi.org/10.1016/j.asr.2019.05.039>, 2019.
- 718 Eyring, Veronika, et al.: Overview of IGAC/SPARC Chemistry-Climate Model
719 Initiative (CCMI) community simulations in support of upcoming ozone and climate
720 assessments, *SPARC newsletter*, 40, 48–66, <https://oceanrep.geomar.de/id/eprint/20227>,
721 2013.
- 722 Forbes, J. M. and Zhang, X.: Quasi-10-day wave in the atmosphere, *J. Geophys. Res.-*
723 *Atmos.*, 120, 11,079–11,089, <https://doi.org/10.1002/2015jd023327>, 2015.
- 724 Forbes, J. M. and Zhang, X.: The quasi-6 day wave and its interactions with solar tides,
725 *J. Geophys. Res.-Space*, 122, 4764–4776, <https://doi.org/10.1002/2017ja023954>, 2017.
- 726 Forbes, J. M., Hagan, M. E., Miyahara, S., Vial, F., Manson, A. H., Meek, C. E., and
727 Portnyagin, Y. I.: Quasi 16-day oscillation in the mesosphere and lower thermosphere,
728 *J. Geophys. Res.-Atmos.*, 100, 9149–9163, <https://doi.org/10.1029/94jd02157>, 1995.
- 729 Forbes, J. M., Zhang, X., Heelis, R., Stoneback, R., Englert, C. R., Harlander, J. M.,
730 Harding, B. J., Marr, K. D., Makela, J. J., and Immel, T. J.: Atmosphere-Ionosphere (A-
731 I) Coupling as Viewed by ICON: Day-to-Day Variability Due to Planetary Wave (PW)-
732 Tide Interactions, *J. Geophys. Res.-Space*, 126, <https://doi.org/10.1029/2020ja028927>,
733 2021.
- 734 Gan, Q., Oberheide, J., and Pedatella, N. M.: Sources, Sinks, and Propagation
735 Characteristics of the Quasi 6-Day Wave and Its Impact on the Residual Mean



- 736 Circulation, *J. Geophys. Res.-Atmos.*, 123, 9152–9170,
737 <https://doi.org/10.1029/2018jd028553>, 2018.
- 738 Gelaro, R., McCarty, W., Suárez, M. J., Todling, R., Molod, A., Takacs, L., Randles, C.
739 A., Darmenov, A., Bosilovich, M. G., Reichle, R., Wargan, K., Coy, L., Cullather, R.,
740 Draper, C., Akella, S., Buchard, V., Conaty, A., Silva, A. M. da, Gu, W., Kim, G.-K.,
741 Koster, R., Lucchesi, R., Merkova, D., Nielsen, J. E., Partyka, G., Pawson, S., Putman,
742 W., Rienecker, M., Schubert, S. D., Sienkiewicz, M., and Zhao, B.: The Modern-Era
743 Retrospective Analysis for Research and Applications, Version 2 (MERRA-2), *J.*
744 *Climate*, 30, 5419–5454, <https://doi.org/10.1175/jcli-d-16-0758.1>, 2017.
- 745 Goncharenko, L. P., Harvey, V. L., Greer, K. R., Zhang, S. -R., and Coster, A. J.:
746 Longitudinally Dependent Low-Latitude Ionospheric Disturbances Linked to the
747 Antarctic Sudden Stratospheric Warming of September 2019, *J. Geophys. Res.-Space*,
748 125, <https://doi.org/10.1029/2020ja028199>, 2020.
- 749 Harvey, V. L., Randall, C. E., Becker, E., Smith, A. K., Bardeen, C. G., France, J. A.,
750 and Goncharenko, L. P.: Evaluation of the Mesospheric Polar Vortices in WACCM, *J.*
751 *Geophys. Res.-Atmos.*, 124, 10626–10645, <https://doi.org/10.1029/2019jd030727>,
752 2019.
- 753 He, M., Chau, J. L., Stober, G., Li, G., Ning, B., and Hoffmann, P.: Relations Between
754 Semidiurnal Tidal Variants Through Diagnosing the Zonal Wavenumber Using a Phase
755 Differencing Technique Based on Two Ground-Based Detectors, *J. Geophys. Res.-*
756 *Atmos.*, 123, 4015–4026, <https://doi.org/10.1002/2018jd028400>, 2018.



- 757 He, M., Yamazaki, Y., Hoffmann, P., Hall, C. M., Tsutsumi, M., Li, G., and Chau, J. L.:
758 Zonal Wave Number Diagnosis of Rossby Wave-Like Oscillations Using Paired
759 Ground-Based Radars, *J. Geophys. Res.-Atmos.*, 125,
760 <https://doi.org/10.1029/2019jd031599>, 2020.
- 761 Hirooka, T.: Normal Mode Rossby Waves as Revealed by UARS/ISAMS Observations,
762 *J. Atmos. Sci.*, 57, 1277–1285, [https://doi.org/10.1175/1520-0469\(2000\)057<1277:NMRWAR>2.0.CO;2](https://doi.org/10.1175/1520-0469(2000)057<1277:NMRWAR>2.0.CO;2), 2000.
- 764 Holdsworth, D. A., Murphy, D. J., Reid, I. M., and Morris, R. J.: Antarctic meteor
765 observations using the Davis MST and meteor radars, *Adv. Space Res.*, 42, 143–154,
766 <https://doi.org/10.1016/j.asr.2007.02.037>, 2008.
- 767 Huang, C., Zhang, S., Chen, G., Zhang, S., and Huang, K.: Planetary Wave
768 Characteristics in the Lower Atmosphere Over Xianghe (117.00°E, 39.77°N), China,
769 Revealed by the Beijing MST Radar and MERRA Data, *J. Geophys. Res.-Atmos.*, 122,
770 9745–9758, <https://doi.org/10.1002/2017jd027029>, 2017.
- 771 Huang, C., Li, W., Zhang, S., Chen, G., Huang, K., and Gong, Y.: Investigation of
772 dominant traveling 10-day wave components using long-term MERRA-2 database,
773 *Earth Planets Space*, 73, 85, <https://doi.org/10.1186/s40623-021-01410-7>, 2021.
- 774 Huang, Y.-Y., Cui, J., Li, H.-J., and Li, C.-Y.: Inter-annual variations of 6.5-day
775 planetary waves and their relations with QBO, *Earth Planet. Phys.*, 6, 135–148,
776 <https://doi.org/10.26464/epp2022005>, 2022.



- 777 Lee, W., Song, I., Kim, J., Kim, Y. H., Jeong, S., Eswarajah, S., and Murphy, D. J.: The
778 Observation and SD-WACCM Simulation of Planetary Wave Activity in the Middle
779 Atmosphere During the 2019 Southern Hemispheric Sudden Stratospheric Warming, J.
780 Geophys. Res.-Space, 126, <https://doi.org/10.1029/2020ja029094>, 2021.
- 781 Lee, W., Lee, C., Kim, J., Kam, H., and Kim, Y. H.: A Modeling Analysis of the
782 Apparent Linear Relation Between Mesospheric Temperatures and Meteor Height
783 Distributions Measured by a Meteor Radar, J. Geophys. Res.-Space, 127,
784 <https://doi.org/10.1029/2021ja029812>, 2022.
- 785 Lee, W., Kim, Y. H., Lee, C., and Wu, Q.: First Comparison of Mesospheric Winds
786 Measured with a Fabry-Perot Interferometer and Meteor Radar at the King Sejong
787 Station (62.2°S, 58.8°W), J. Astron. Space Sci.,
788 <https://doi.org/10.5140/JASS.2018.35.4.235>, 2018
- 789 Li, W., Huang, C., and Zhang, S.: Global characteristics of the westward-propagating
790 quasi-16-day wave with zonal wavenumber 1 and the connection with the 2012/2013
791 SSW revealed by ERA-Interim, Earth Planets Space, 73, 113,
792 <https://doi.org/10.1186/s40623-021-01431-2>, 2021.
- 793 Lindzen, R. S., Farrell, B., and Tung, K.-K.: The Concept of Wave Overreflection and
794 Its Application to Baroclinic Instability, J. Atmos. Sci., 37, 44–63,
795 [https://doi.org/10.1175/1520-0469\(1980\)037<0044:tcowoa>2.0.co;2](https://doi.org/10.1175/1520-0469(1980)037<0044:tcowoa>2.0.co;2), 1980.
- 796 Liu, G., Janches, D., Lieberman, R. S., Moffat-Griffin, T., Mitchell, N. J., Kim, J., and
797 Lee, C.: Wind Variations in the Mesosphere and Lower Thermosphere Near 60°S



- 798 Latitude During the 2019 Antarctic Sudden Stratospheric Warming, *J. Geophys. Res.-*
799 *Space*, 126, <https://doi.org/10.1029/2020ja028909>, 2021.
- 800 Liu, G., Janches, D., Ma, J., Lieberman, R. S., Stober, G., Moffat-Griffin, T., Mitchell,
801 N. J., Kim, J., Lee, C., and Murphy, D. J.: Mesosphere and Lower Thermosphere Winds
802 and Tidal Variations During the 2019 Antarctic Sudden Stratospheric Warming, *J.*
803 *Geophys. Res.-Space*, 127, <https://doi.org/10.1029/2021ja030177>, 2022.
- 804 Luo, J., Gong, Y., Ma, Z., Zhang, S., Zhou, Q., Huang, C., Huang, K., Yu, Y., and Li,
805 G.: Study of the Quasi 10-Day Waves in the MLT Region During the 2018 February
806 SSW by a Meteor Radar Chain, *J. Geophys. Res.-Space*, 126,
807 <https://doi.org/10.1029/2020ja028367>, 2021.
- 808 Ma, Z., Gong, Y., Zhang, S., Xiao, Q., Xue, J., Huang, C., and Huang, K.:
809 Understanding the Excitation of Quasi-6-Day Waves in Both Hemispheres During the
810 September 2019 Antarctic SSW, *J. Geophys. Res.-Atmos.*, 127,
811 <https://doi.org/10.1029/2021jd035984>, 2022.
- 812 Marsh, D. R., Mills, M. J., Kinnison, D. E., Lamarque, J.-F., Calvo, N., and Polvani, L.
813 M.: Climate Change from 1850 to 2005 Simulated in CESM1(WACCM), *J. Climate*,
814 26, 130509150556003, <https://doi.org/10.1175/jcli-d-12-00558.1>, 2013.
- 815 Matsuno, T.: Vertical Propagation of Stationary Planetary Waves in the Winter
816 Northern Hemisphere, *J. Atmos. Sci.*, 27, 871–883, [https://doi.org/10.1175/1520-0469\(1970\)027<0871:vpospw>2.0.co;2](https://doi.org/10.1175/1520-0469(1970)027<0871:vpospw>2.0.co;2), 1970.



- 818 Matthias, V. and Ern, M.: On the origin of the mesospheric quasi-stationary planetary
819 waves in the unusual Arctic winter 2015/2016, *Atmos. Chem. Phys.*, 18, 4803–4815,
820 <https://doi.org/10.5194/acp-18-4803-2018>, 2018.
- 821 McFarlane, N. A.: The Effect of Orographically Excited Gravity Wave Drag on the
822 General Circulation of the Lower Stratosphere and Troposphere, *J. Atmos. Sci.*, 44,
823 1775–1800, [https://doi.org/10.1175/1520-0469\(1987\)044<1775:teooeg>2.0.co;2](https://doi.org/10.1175/1520-0469(1987)044<1775:teooeg>2.0.co;2), 1987.
- 824 Meyer, C. K. and Forbes, J. M.: A 6.5-day westward propagating planetary wave:
825 Origin and characteristics, *J. Geophys. Res.-Atmos.*, 102, 26173–26178,
826 <https://doi.org/10.1029/97jd01464>, 1997.
- 827 Mitra, G., Guharay, A., Batista, P. P., and Buriti, R. A.: Impact of the September 2019
828 Minor Sudden Stratospheric Warming on the Low-Latitude Middle Atmospheric
829 Planetary Wave Dynamics, *J. Geophys. Res.-Atmos.*, 127,
830 <https://doi.org/10.1029/2021jd035538>, 2022.
- 831 Palmer, T. N.: Properties of the Eliassen-Palm Flux for Planetary Scale Motions, *J.*
832 *Atmos. Sci.*, 39, 992–997, [https://doi.org/10.1175/1520-0469\(1982\)039<0992:potepf>2.0.co;2](https://doi.org/10.1175/1520-0469(1982)039<0992:potepf>2.0.co;2), 1982.
- 834 Qin, Y., Gu, S., Dou, X., Gong, Y., Chen, G., Zhang, S., and Wu, Q.: Climatology of
835 the Quasi-6-Day Wave in the Mesopause Region and Its Modulations on Total Electron
836 Content During 2003–2017, *J. Geophys. Res.-Space*, 124, 573–583,
837 <https://doi.org/10.1029/2018ja025981>, 2019.



- 838 Qin, Y., Gu, S., Teng, C., Dou, X., Yu, Y., and Li, N.: Comprehensive Study of the
839 Climatology of the Quasi-6-Day Wave in the MLT Region Based on Aura/MLS
840 Observations and SD-WACCM-X Simulations, *J. Geophys. Res.-Space*, 126,
841 <https://doi.org/10.1029/2020ja028454>, 2021.
- 842 Reynolds, R. W., Rayner, N. A., Smith, T. M., Stokes, D. C., and Wang, W.: An
843 Improved In Situ and Satellite SST Analysis for Climate, *J. Climate*, 15, 1609–1625,
844 [https://doi.org/10.1175/1520-0442\(2002\)015<1609:aiisas>2.0.co;2](https://doi.org/10.1175/1520-0442(2002)015<1609:aiisas>2.0.co;2), 2002.
- 845 Rhodes, C. T., Limpasuvan, V., and Orsolini, Y. J.: Eastward-Propagating Planetary
846 Waves Prior to the January 2009 Sudden Stratospheric Warming, *J. Geophys. Res.-*
847 *Atmos.*, 126, <https://doi.org/10.1029/2020jd033696>, 2021.
- 848 Richter, J. H., Sassi, F., and Garcia, R. R.: Toward a Physically Based Gravity Wave
849 Source Parameterization in a General Circulation Model, *J. Atmos. Sci.*, 67, 136–156,
850 <https://doi.org/10.1175/2009jas3112.1>, 2010.
- 851 Salby, M. L.: Rossby Normal Modes in Nonuniform Background Configurations. Part I:
852 Simple Fields, *J. Atmos. Sci.*, 38, 1803–1826, [https://doi.org/10.1175/1520-](https://doi.org/10.1175/1520-0469(1981)038<1803:rnminb>2.0.co;2)
853 [0469\(1981\)038<1803:rnminb>2.0.co;2](https://doi.org/10.1175/1520-0469(1981)038<1803:rnminb>2.0.co;2), 1981a.
- 854 Salby, M. L.: Rossby Normal Modes in Nonuniform Background Configurations. Part
855 II. Equinox and Solstice Conditions, *J. Atmos. Sci.*, 38, 1827–1840,
856 [https://doi.org/10.1175/1520-0469\(1981\)038<1827:rnminb>2.0.co;2](https://doi.org/10.1175/1520-0469(1981)038<1827:rnminb>2.0.co;2), 1981b.



- 857 Salby, M. L.: Survey of planetary-scale traveling waves: The state of theory and
858 observations, *Rev. Geophys.*, 22, 209–236, <https://doi.org/10.1029/rg022i002p00209>,
859 1984.
- 860 Sassi, F., McCormack, J. P., Tate, J. L., Kuhl, D. D., and Baker, N. L.: Assessing the
861 impact of middle atmosphere observations on day-to-day variability in lower
862 thermospheric winds using WACCM-X, *J. Atmos. Sol.-Terr. Phys.*, 212, 105486,
863 <https://doi.org/10.1016/j.jastp.2020.105486>, 2021.
- 864 Sato, K., Yasui, R., and Miyoshi, Y.: The Momentum Budget in the Stratosphere,
865 Mesosphere, and Lower Thermosphere. Part I: Contributions of Different Wave Types
866 and In Situ Generation of Rossby Waves, *J. Atmos. Sci.*, 75, 3613–3633,
867 <https://doi.org/10.1175/jas-d-17-0336.1>, 2018.
- 868 Schwartz, M. J., Lambert, A., Manney, G. L., Read, W. G., Livesey, N. J., Froidevaux,
869 L., Ao, C. O., Bernath, P. F., Boone, C. D., Cofield, R. E., Daffer, W. H., Drouin, B. J.,
870 Fetzer, E. J., Fuller, R. A., Jarnot, R. F., Jiang, J. H., Jiang, Y. B., Knosp, B. W.,
871 Krüger, K., Li, J. -L. F., Mlynczak, M. G., Pawson, S., Russell, J. M., Santee, M. L.,
872 Snyder, W. V., Stek, P. C., Thurstans, R. P., Tompkins, A. M., Wagner, P. A., Walker,
873 K. A., Waters, J. W., and Wu, D. L.: Validation of the Aura Microwave Limb Sounder
874 temperature and geopotential height measurements, *J. Geophys. Res.-Atmos.* 1984
875 2012, 113, <https://doi.org/10.1029/2007jd008783>, 2008.
- 876 Song, B.-G., Chun, H.-Y., and Song, I.-S.: Role of Gravity Waves in a Vortex-Split
877 Sudden Stratospheric Warming in January 2009, *J. Atmos. Sci.*, 77, 3321–3342,
878 <https://doi.org/10.1175/jas-d-20-0039.1>, 2020.



- 879 Thorncroft, C. D., Hoskins, B. J., and McIntyre, M. E.: Two paradigms of baroclinic-
880 wave life-cycle behaviour, *Q. J. Roy. Meteor. Soc.*, 119, 17–55,
881 <https://doi.org/10.1002/qj.49711950903>, 1993.
- 882 Torrence, C. and Compo, G. P.: A Practical Guide to Wavelet Analysis, *B. Am.*
883 *Meteorol. Soc.*, 79, 61–78, [https://doi.org/10.1175/1520-](https://doi.org/10.1175/1520-0477(1998)079<0061:apgtwa>2.0.co;2)
884 [0477\(1998\)079<0061:apgtwa>2.0.co;2](https://doi.org/10.1175/1520-0477(1998)079<0061:apgtwa>2.0.co;2), 1998.
- 885 Walker, S. N., Sahraoui, F., Balikhin, M. A., Belmont, G., Pinçon, J. L., Rezeau, L.,
886 Alleyne, H., Cornilleau-Wehrin, N., and André, M.: A comparison of wave mode
887 identification techniques, *Ann. Geophys.*, 22, 3021–3032,
888 <https://doi.org/10.5194/angeo-22-3021-2004>, 2004.
- 889 Wang, J. C., Palo, S. E., Forbes, J. M., Marino, J., Moffat-Griffin, T., and Mitchell, N.
890 J.: Unusual Quasi 10-Day Planetary Wave Activity and the Ionospheric Response
891 During the 2019 Southern Hemisphere Sudden Stratospheric Warming, *J. Geophys.*
892 *Res.-Space*, 126, <https://doi.org/10.1029/2021ja029286>, 2021.
- 893 Yamazaki, Y. and Matthias, V.: Large-Amplitude Quasi-10-Day Waves in the Middle
894 Atmosphere During Final Warmings, *J. Geophys. Res.-Atmos.*, 124, 9874–9892,
895 <https://doi.org/10.1029/2019jd030634>, 2019.